Chemical Engineering Journal 442 (2022) 136214

Contents lists available at ScienceDirect

Chemical Engineering Journal

journal homepage: www.elsevier.com/locate/cej

Synergistic tailoring of band structure and charge carrier extraction in "green" core/shell quantum dots for highly efficient solar energy conversion

Li Xia [a], Xin Tong [a,b,*], Xin Li [a], Ali Imran Channa [a], Yimin You [a], Zhihang Long [a], Alberto Vomiero [c,d,*], Zhiming M. Wang [a,e,*]

[a] Institute of Fundamental and Frontier Sciences, University of Electronic Science and Technology of China, Chengdu 610054, PR China
[b] Yangtze Delta Region Institute (Huzhou), University of Electronic Science and Technology of China, Huzhou 313001, PR China
[c] Division of Materials Science, Department of Engineering Sciences and Mathematics, Luleå University of Technology, Luleå SE-97187, Sweden
[d] Department of Molecular Sciences and Nanosystems, Ca' Foscari University of Venice, Via Torino 155, Venezia Mestre 30170, Italy
[e] Institute for Advanced Study, Chengdu University, Chengdu 610106, PR China

ARTICLE INFO

Keywords:
Colloidal quantum dots
Environment-friendly
Core/shell system
Synergistic optoelectronic engineering
Solar hydrogen evolution

ABSTRACT

Environment-friendly colloidal core/shell quantum dots (QDs) with controllable optoelectronic characteristics are promising building blocks for future commercial solar technologies. Herein, we synergistically tailor the electronic band structure and charge carrier extraction of eco-friendly $AgInS_2$ (AIS)/ZnS core/shell QDs via Mn-alloying and Cu-doping in the core and shell, respectively. It is demonstrated that the Mn-alloying in AIS core can broaden the band gap to facilitate delocalization of photogenerated electrons into the shell and further incorporation of Cu in the ZnS shell enables the creation of Cu-related states that capture the photogenerated holes from core, thus leading to charge carrier recombination and accelerated transfer of photogenerated electrons in the core/shell QDs. As-prepared Mn-AIS/ZnS@Cu QDs were assembled as light harvesters in a photoelectrochemical (PEC) device for light-driven hydrogen evolution, delivering a maximum photocurrent density of ~ 6.4 mA cm^{-2} with superior device stability under standard one sun irradiation (AM 1.5G, 100 mW cm^{-2}). Our findings highlight that simultaneously engineering the band alignment and charge carrier dynamics of "green" core/shell QDs endow the feasibility to design future high-efficiency and durable solar hydrogen production systems.

1. Introduction

Nowadays, the global energy needs are still mainly fulfilled by the consumption of fossil fuels including coal, crude oil, and natural gas etc., which are the sources of greenhouse effect and environmental pollution. [1] Hence, developing sustainable and renewable energy sources is supposed to be one of the most promising approaches to relieve the growing worldwide energy demand and address various environmental issues.[2] Particularly, solar energy has demonstrated earth-abundant, safe, renewable and clean merits and is considered as an attractive sustainable energy source to be exploited.[3] Towards this effort, solar-driven photoelectrochemical (PEC) cells have been developed to utilize solar energy to produce hydrogen, which exhibits no carbon emissions and can act as future energy carrier alternative to conventional fossil fuels.[4–6].

Generally, an attractive PEC hydrogen production system requires the use of cheap, environmentally friendly and sustainable materials to achieve a low-cost manufacturing process and high-efficiency solar-to-hydrogen conversion.[7–9] Wide-band gap semiconductor metal oxides (e.g. ZnO, TiO_2, NiO etc.) are widely used as light-absorbing materials to construct the working electrodes (photoanodes or photocathodes) of PEC cells mainly due to their cost-effectiveness, high stability and appropriate band alignment for water splitting.[10–14] However, the wide-band gap of conventional photoelectrodes limits their light absorbance to ultraviolet (UV) range that merely accounts for ~ 4% of solar spectrum.[15] In order to improve the solar energy conversion efficiency of PEC cells, narrow-bandgap semiconductors possessing broad light harvesting and effective charge carrier separation/transfer

* Corresponding authors.
E-mail addresses: xin.tong@uestc.edu.cn (X. Tong), alberto.vomiero@unive.it (A. Vomiero), zhmwang@uestc.edu.cn (Z.M. Wang).

https://doi.org/10.1016/j.cej.2022.136214
Received 30 January 2022; Received in revised form 22 March 2022; Accepted 3 April 2022
Available online 5 April 2022

abilities are desirable photosensitizers to modify the wide-band gap working electrodes for enhanced device performance.[16].

Colloidal quantum dots (QDs) have received widespread attention as light-sensitive building blocks in solar-driven PEC systems because of their size/composition-tunable optical properties.[17] However, state-of-the-art high performance QDs-PEC cells are still mainly based on the highly toxic IV-VI and II-VI group Pb/Cd- chalcogenide QDs, which are very harmful to the human health and environment.[18–23] Recently, I-III-VI group QDs (e.g. CuInS/Se and AgInSe/S etc.) are regarded as favorable substitutes of Pb and Cd-based QDs due to their environmental friendliness and excellent optical properties including wide photoluminescence tunability, broadband light absorption, large Stokes shift, and high luminescence efficiency, which have been widely applied in various optoelectronic devices including light-emitting diodes (LEDs), solar cells, luminescent solar concentrators (LSCs) and PEC cells.[24–37].

Among various eco-friendly I-III-VI QDs, $AgInS_2$ (AIS) QDs exhibiting narrow band gap (bulk value ~ 1.9 eV) with broad absorbance from UV to near-infrared (NIR) region are potential candidates for achieving high-efficiency solar energy conversion. However, bare AIS QDs usually suffer from abundant surface defects and high environment-related sensitivity (such as humidity and light), which can hamper their optical properties and chemical stability.[38] These undesirable issues can be addressed by growing an inorganic protecting shell material (commonly using ZnS) on the AIS core QDs to construct a core–shell structure,[39–40] in which the ZnS shell enables the effective passivation of the core and enhances the optical properties as well as the chemical stability of AIS QDs.[41] Such eco-friendly AIS/ZnS core/shell QDs can act as efficient light absorbers/emitters and have demonstrated variable potential optoelectronic and biological applications including LEDs, solar cells, and bioimaging etc.[42–44] However, owing to the type-I electronic band structure of AIS/ZnS core/shell QDs, both the electrons and holes are readily confined in the core QDs, which hinder the photo-excited charge separation/transfer and carrier extraction from core to shell region, consequently leading to the limited charge injection from QDs into semiconductor metal oxides, resulting in low-efficiency solar energy conversion devices (e.g. light-driven QDs-PEC cells).

Tuning the band structure of core QDs with optically active transition metals may optimize the charge separation and transfer kinetics in such core/shell QDs.[45–47] For example, our previous studies of similar I-III-VI group $CuInS_2$/ZnS core/shell structured QDs have shown that Mn-alloying in the $CuInS_2$ core facilitates the electron delocalization in the ZnS shell, thereby effectively prolonging the exciton lifetime of QDs for promoted charge carriers separation and transfer in the QDs-based solar energy conversion applications.[48] In addition, doping the shell with metal cations can create impurity states to trap light-excited holes from the core and improve the efficiency of light-excited electron transfer, by inhibiting the electron-hole recombination processes in the core/shell QDs.[49] For instance, Hong et al. have reported that the carrier recombination rate of InP/ZnS core/shell QDs can be effectively reduced with Cu shell doping owing to decreased electron-hole overlap through hole capturing via the Cu impurity sites in ZnS shell, which is an effective strategy towards environment-friendly QDs-based solar technologies.[50] Therefore, we can infer that simultaneously modifying the eco-friendly AIS/ZnS core/shell QDs is able to tailor both the electronic band structure and charge carriers' kinetics for achieving high performance QDs-solar energy conversion devices. To the best of our knowledge, there is no literature reporting the synergistic modification of core and shell materials in eco-friendly AIS/ZnS QDs and the application in solar-driven PEC hydrogen generation is still lacking.

In this work, we developed a new type of eco-friendly Mn-AIS/ZnS@Cu core/shell QDs via synergistically engineering the band structure and charge carrier extraction of eco-friendly AIS/ZnS core/shell QDs by using Mn core alloying and Cu shell doping. The Mn alloying of AIS core QDs results in enlarged band gap and delocalized electrons to the ZnS shell, as evidenced by the blue-shifted emission/absorption spectra and extended photoluminescence (PL) lifetime of QDs. After Cu-doping in the ZnS shell, the holes in the core were effectively captured by Cu^+ states in the shell, thus leading to the inhibited charge recombination of holes and electrons in the core/shell QDs. We found that such simultaneous modification of the core and shell of AIS/ZnS QDs can not only tune the optical properties of QDs, but also improve the charge dynamics of corresponding QDs-PEC cells for largely enhanced device performance and stability. Our results reveal that simultaneously tailoring the band structure and charger extraction processes in "green" core/shell QDs can lead to eco-friendly, highly efficient and robust solar energy conversion devices.

2. Experimental section

2.1. Materials

Silver nitrate ($AgNO_3$) (≥99.99%), manganese acetate ($Mn(Ac)_2$), copper(II) chloride ($CuCl_2$), indium(III) acetate ($In(Ac)_3$) (≥99.99%), sulfur (S) (≥99.99%), 1-dodecanethiol (DDT), oleic acid (OA), ethanol, toluene, methanol, hexadecyl trimethyl ammonium bromide (CTAB, 90%), 1-octadecene (ODE), sodium stearate $Na(C_{18}H_{35}O_2)$, sodium sulfide nonahydrate, ($Na_2S{\cdot}9H_2O$), zinc acetate dihydrate ($Zn(Ac)_2{\cdot}2H_2O$), sodium sulfite (Na_2SO_3) and oleylamine (OLA) were purchased from Sigma-Aldrich. ZrO_2 (99.99%) was purchased from Aladdin. Titania paste (18 NR-AO) was purchased from Dyesol (Queanbeyan, Australia). Ti-Nanoxide BL/SC was obtained from Solaronix. All chemicals were used without further purification.

2.2. Preparation of Cu precursors

8 mmol of sodium stearate was mixed with 44.8 mL of methanol and heated to ~ 60–65 °C in N_2 atmosphere until it turns to be clear.[51] Under vigorous stirring, 4 mmol of copper chloride in 16.8 mL of methanol solution was injected dropwise to sodium stearate solution to produce copper stearate. Such precipitated copper (II) stearate was slowly flocculated and maintained at 60 °C for 4 h, washing with methanol and dried at 60 °C for 4 h in vacuum.

2.3. Synthesis of AIS/ZnS and Mn-AIS/ZnS core/shell QDs

Mn-alloyed AIS/ZnS core/shell QDs were prepared by a reported wet-chemical method with modifications.[52] Typically, 0.1 mmol $Mn(Ac)_2$, 0.05 mmol $AgNO_3$, 0.05 mmol $In(Ac)_3$, 0.2 mL of OA, and 5 mL of ODE were loaded into a three-neck flask and degassed at room temperature. The temperature was raised to at 120 ℃ and 0.2 mL of DDT was then quickly injected into the reaction mixture. Afterwards, S (0.3 mmol) dissolved in OLA (1.0 mL) was injected at the same temperature to induce the growth of Mn-AIS QDs, which was maintained for 20 min. Subsequently, 1 mL of 0.2 M $Zn(Ac)_2{\cdot}2H_2O$ dissolved in ODE/OA (with ODE/OA ratio of 4/1) was injected into the reaction solution and the temperature was raised to 180 °C for 30 min to grow the shell. The as-synthesized Mn-alloyed AIS/ZnS core/shell QDs with above-mentioned Mn/Ag molar feed ratio of 2 are named as 2-Mn-AIS/ZnS QDs. In parallel, to explore the properties of QDs with different added Mn contents, we also synthesized other QDs with different Mn contents (Mn/Ag molar feed ratio = 0, 0.5, 1, 3), which are named as Mn:AIS/ZnS QDs (including AIS/ZnS, 0.5-Mn-AIS/ZnS, 1-Mn-AIS/ZnS and 3-Mn-AIS/ZnS).

2.4. Synthesis of Mn-AIS/ZnS@Cu and AIS/ZnS@Cu core/shell QDs

For Cu shell doping in MnAIS/ZnS core/shell QDs, 0.1 M copper stearate (Cu/In-Ag weight feed ratio: 0, 0.5, 0.75) in ODE was added to the optimized 2-Mn-AIS/ZnS core/shell QDs reaction solution at 180 °C and maintained for 1 h, as-prepared QDs are named as Mn:AIS/ZnS:Cu (including 2-Mn-AIS/ZnS, 2-Mn-AIS/ZnS@0.5Cu and 2-Mn-AIS/

ZnS@0.75Cu) QDs. The AIS/ZnS@Cu QDs were prepared using identical method of 2-Mn-AIS/ZnS@0.5Cu sample but without the introduction of the $Mn(Ac)_2$ precursor.

2.5. Preparation of QDs-sensitized PEC device

TiO_2 films were first prepared by a tape-casting technique and the thickness of the film can be controlled by varying the tape thickness. Electrophoretic deposition (EPD) technique was then employed to deposit the synthesized QDs into the TiO_2 mesoporous film.[48] In a typical process, two pieces of as-prepared TiO_2/FTO electrodes were vertically soaked in the QDs solution with a 1 cm distance. A direct current bias of 200 V was applied for 120 min and the deposited QDs-TiO_2 photoanodes were subsequently washed with toluene and dried in N_2 flow. The photoanodes were then coated with 5 ZnS passivation layers by using successive ionic layer adsorption and reaction (SILAR) method and treated with CTAB for ligand exchange.[37] The QDs-photoanodes after SILAR treatment were placed in the tubular furnace with pumping for 30 min, annealed at 120 °C for 30 min and cooled to room temperature for further measurement. The fabrication process was completed by covering the surface of photoanodes with insulating epoxy, leaving a circular region (~0.10 cm^2) as the active area.

2.6. Characterization

Field emission SEM (ZEISS Gemini SEM 300) and TEM (FEI TECNAI G2 F20 TEM) are employed to study the morphology and structure of samples. The crystal structure and components of samples were characterized by XPS (ESCALAB 250Xi analyzer) and XRD (Bruker D8 advanced diffractometer, Cu K_α radiation). UV–vis-NIR spectrophotometer (Varian Cary 5000) is used to test the absorption spectrum of samples. A spectrophotometer (FLS 920 fluorescence spectrometer) was used to measure the steady-state PL spectra (410 nm excitation) and time-resolved PL lifetime (450 nm excitation) of QDs and QDs-sensitized photoelectrodes. Escalab 250xi spectrometer with He I source (21.21 eV) is used for UPS measurements of samples. The yield of hydrogen in the QDs-PEC system is detected by a gas chromatography system (Shimadzu GC-2014).

2.7. PEC measurements of QDs-based devices

An electrochemical workstation (PARSTAT 3000A-DX) coupled with a AAA solar simulator (SAN-EI, XES-50S1) were used to assess the performance of the QDs-based PEC devices. LSV and J-t curves were scanned (scanning rate of 0.02 V/s) in the traditional three-electrode PEC system with electrolyte of 0.25 M Na_2S and 0.35 M Na_2SO_3, in which QDs/TiO_2 FTO photoanode was used as working electrode, Pt foil was used as counter electrode and Ag/AgCl was used as reference electrode.

To estimate the IPCE values, monochromatic optical filters (Edmund Optics) with different wavelengths (380 nm, 420 nm, 460 nm, 510 nm, 550 nm, 600 nm, 660 nm, 700 nm, 760 nm, 840 nm and 930 nm) were placed in front of the solar simulator to measure the *J-V* curves of the QD-PEC device with scanning voltages from −0.5 to 1.0 V vs. RHE. For each optical filter, the incident radiation intensity at the position of sample was measured by Newport power-meter. The IPCE values were calculated by the formula:

$$\mathrm{IPCE} = \frac{1240 \times \mathrm{J}}{\lambda \times \mathrm{I}_{\mathrm{light}}} \times 100 \quad (1)$$

Where J represents the measured saturated photocurrent density at wavelength of λ (nm, incident monochromatic light) and I_{light} refers to the incident light power density.

Faradaic Efficiency was calculated by the equation:

$$\mathrm{FE} = \frac{\mathrm{V}_{(\mathrm{experimental\ gas})}}{\mathrm{V}_{(\mathrm{theoretical\ gas})}} \quad (2)$$

Where $V_{(experimental\ gas)}$ and $V_{(theoretical\ gas)}$ refer to the experimental and theoretical estimated volumes of H_2 gas, respectively. $V_{(theoretical\ gas)}$ is calculated through J-t curves analysis for AIS/ZnS and Mn-AIS/ZnS@Cu core/shell QDs-based PEC cells (**Figure S17**).

Transient PL lifetime calculation and fitting: The average lifetimes (τ_{av}) of QD samples were fitted and calculated from the equation:

$$\tau_{av} = \frac{a_1\tau_1^2 + a_2\tau_2^2 + a_3\tau_3^2}{a_1\tau_1 + a_2\tau_2 + a_3\tau_3} \quad (3)$$

Where a_1, a_2, and a_3 are the fitting coefficients and τ_1, τ_2, and τ_3 are the characteristic lifetimes, respectively.

3. Results and discussion

3.1. Synthesis and structural characterization of Mn-AIS/ZnS@Cu QDs

A facile heat-up method was used to synthesize the AIS/ZnS, Mn-AIS/ZnS and Mn-AIS/ZnS@Cu core/shell QDs, as illustrated by the schematic diagram in Fig. 1**a**. Typically, the growth processes for such core/shell QDs are comprised of three steps: (i) preparation of AIS and Mn-AIS core QDs; (ii) coating of ZnS shell on core QDs and (iii) incorporation of Cu dopant in the ZnS shell. Particularly, AIS/ZnS and Mn-AIS/ZnS core/shell QDs were synthesized as reference samples for comparison. Fig. 1**b-d** show the transmission electron microscope (TEM) images with inset size distribution for AIS/ZnS, Mn-AIS/ZnS, Mn-AIS/ZnS@Cu core/shell QDs, displaying near-spherical shapes with average particle sizes of ~(4.9 ± 0.3), (4.9 ± 0.6) and (4.9 ± 0.4) nm, respectively. It is revealed that the Mn-alloying and subsequent Cu doping have no significant influence on the particle sizes of AIS/ZnS core/shell QDs.

As exhibited in **Figure S1a**, the high-resolution TEM (HR-TEM) image for AIS/ZnS QDs depicts well-resolved lattice fringe spacing of a typical AIS/ZnS core/shell structure, which is almost indexed to the (1 1 1) plane of zinc blende (ZB) ZnS and indicates the formation of relatively thick ZnS shell on AIS core QDs. In parallel, the lattice spacings in HR-TEM images of both Mn-AIS/ZnS (**Figure S1b**) and Mn-AIS/ZnS@Cu QDs (Fig. 1**e**) are also nearly indexed to the (1 1 1) plane of ZB ZnS, which is the main crystalline phase in all the core/shell QDs owing to the growth of thick ZnS shell. However, the core/shell boundary cannot be clearly distinguished from the HRTEM images due to small sized QDs. X-ray diffraction (XRD) patterns were further measured to investigate the crystalline structures of QDs, as shown in Fig. 1**f** and **Figure S2**. The XRD pattern for AIS/ZnS QDs in Fig. 1**f** exhibits three distinct diffraction peaks close to the characteristic planes of ZnS (JCPDS # 05–0556). After Mn-alloying of AIS core QDs, the XRD patterns of the corresponding Mn-AIS/ZnS core/shell QDs still show diffraction peaks similar to AIS/ZnS QDs, which is consistent with the HR-TEM analysis. To demonstrate the successful Mn-alloying in AIS core QDs, we measured the XRD patterns of AIS and Mn-AIS core QDs, as exhibited in **Figure S2**. As compared to the XRD profile of AIS core QDs, three distinctive diffraction peaks of Mn-AIS core QDs are located between $AgInS_2$ (JCPDS # 01–075-0117) and MnS (JCPDS # 40–1288), confirming the successful alloying of Mn in AIS QDs. In contrast, the XRD pattern of Mn-AIS/ZnS@Cu QDs exhibited inconspicuous variation compared to that of the Mn-AIS/ZnS QDs, which is attributed to the low concentration of introduced Cu dopants in the ZnS shell.

We then conducted high-resolution X-ray photoelectron spectroscopy (HR-XPS) measurements to detect the chemical compositions of Mn-AIS/ZnS@Cu QDs. Fig. 1**g** and **Figure S3** exhibit the characteristic peaks in HR-XPS spectra, which demonstrate the presence of Mn, Ag, In, S, Zn and Cu in as-prepared Mn-AIS/ZnS@Cu QDs. To quantify the content of each element, we further carried out the inductively coupled

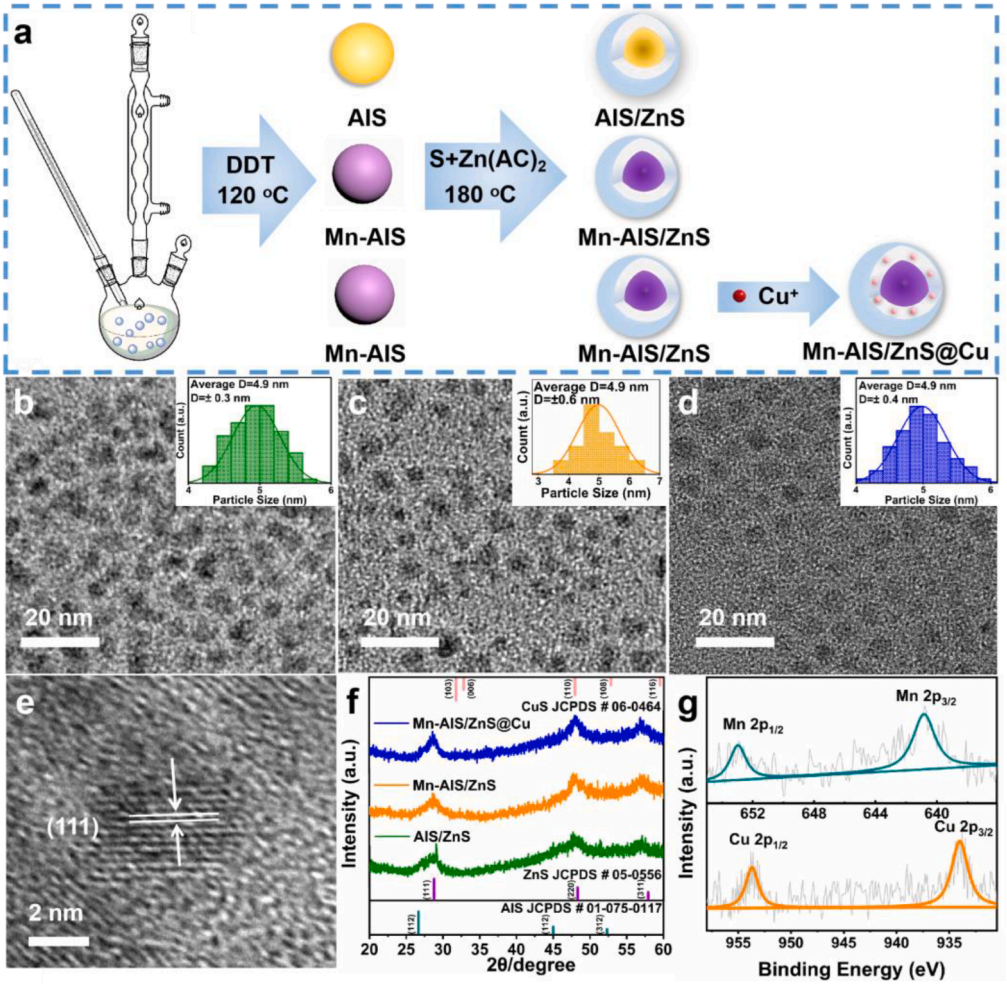

Fig. 1. (a) Schematic illustration of synthesizing Mn-AIS/ZnS@Cu QDs. TEM images and size distribution (inset photographs) of (b) AIS/ZnS, (c) Mn-AIS/ZnS and (d) Mn-AIS/ZnS@Cu QDs. (e) HR-TEM image of Mn-AIS/ZnS@Cu QDs. (f) XRD patterns of AIS/ZnS, Mn-AIS/ZnS and Mn-AIS/ZnS@Cu QDs. (g) HR-XPS spectra of Mn 2p and Cu 2p core levels in Mn-AIS/ZnS@Cu QDs.

plasma-optical emission spectrometry (ICP-OES) tests (Table S1), wherein the molar percentages of Mn, Ag, In, S, Zn and Cu were calculated to be ~ 6.7%, 8.9%, 14.3%, 43.2%, 25.3% and 1.6%, respectively. The results of the elemental analysis reported above indicate the successful realization of Mn core alloying and Cu shell doping in AIS/ZnS core/shell QDs.

3.2. Optical properties of Mn-AIS/ZnS@Cu QDs

Ultraviolet–visible (UV–vis) absorption spectra of AIS/ZnS, Mn-AIS/ZnS, Mn-AIS/ZnS@Cu QDs in solution are exhibited in Fig. 2**a**. Following Mn incorporation, as compared to AIS/ZnS QDs, the Mn-AIS/ZnS QDs showed blue-shifted absorption due to the alloying effect of wide band gap MnS (bulk, ~3.1 eV) in host material of narrow band gap AIS (bulk, ~1.9 eV [53]), thus broadening the band gap of consequent Mn-AIS-based core/shell QDs. This conclusion is also demonstrated by the blue-shifted absorption spectra of Mn-AIS core QDs with respect to the AIS core QDs (**Figure S4**). However, with subsequent Cu-doping in the ZnS shell, as-prepared Mn-AIS/ZnS@Cu QDs presented very slight red-shifted absorption (inset in Fig. 2**a**), which is ascribed to the relatively narrower band gap of Cu-doped ZnS shell materials than that of the pristine ZnS.[54] We further measured the absorption spectra of QDs with different Mn and Cu concentrations, as depicted in **Figure S5**. It is also revealed that increasing Mn contents in Mn-AIS/ZnS QDs can result in successive blue-shifted absorption, while further increasing Cu dopants in ZnS shell can lead to mild red-shifted absorption of Mn-AIS/ZnS@Cu QDs. As exhibited in Fig. 2**b**, by using Tauc plot method, the optical band gaps for AIS/ZnS, Mn-AIS/ZnS and Mn-AIS/ZnS@Cu QDs are roughly estimated to be ~ 2.11, ~2.45, and ~ 2.35 eV, respectively. The obtained values are in accordance with the band gap variation trends of QDs caused by Mn core alloying and Cu shell doping.

PL spectra of QDs in solution were measured and displayed in Fig. 2**c**. As compared to the pristine AIS/ZnS QDs with an emission peak at ~ 710 nm, the Mn-AIS/ZnS QDs exhibited a blue-shifted emission peak at ~ 684 nm. This is ascribed to the enlarged band gap of Mn-alloyed AIS core QDs that emit at shorter wavelength, which is in accordance with the blue-shifted absorption spectra of AIS/ZnS QDs after Mn alloying. In addition, the emission peak position of Mn-AIS/ZnS QDs is tunable by varying the alloyed Mn contents in the Mn-AIS core QDs, as shown in **Figure S6a**. In comparison to Mn-AIS/ZnS QDs, incorporation of Cu in the ZnS shell (sample Mn-AIS/ZnS@Cu) results in a slight red-shift of PL emission peak from ~ 684 to ~ 692 nm. This is owing to the formation of the Cu^{+} states in the ZnS shell, which efficiently capture the photo-excited holes from the core QDs, followed by radiative recombination with the electrons in the core QD's conduction band, thereby causing the red shift of PL peak.[55] Moreover, with increasing concentration of Cu dopants, the emission peak can gradually red-shift to longer wavelengths, as shown in **Figure S6b**.

Time-resolved PL spectra of QDs in solution were acquired and the normalized PL intensity decay is reported in Fig. 2**d-f**. We fitted the PL

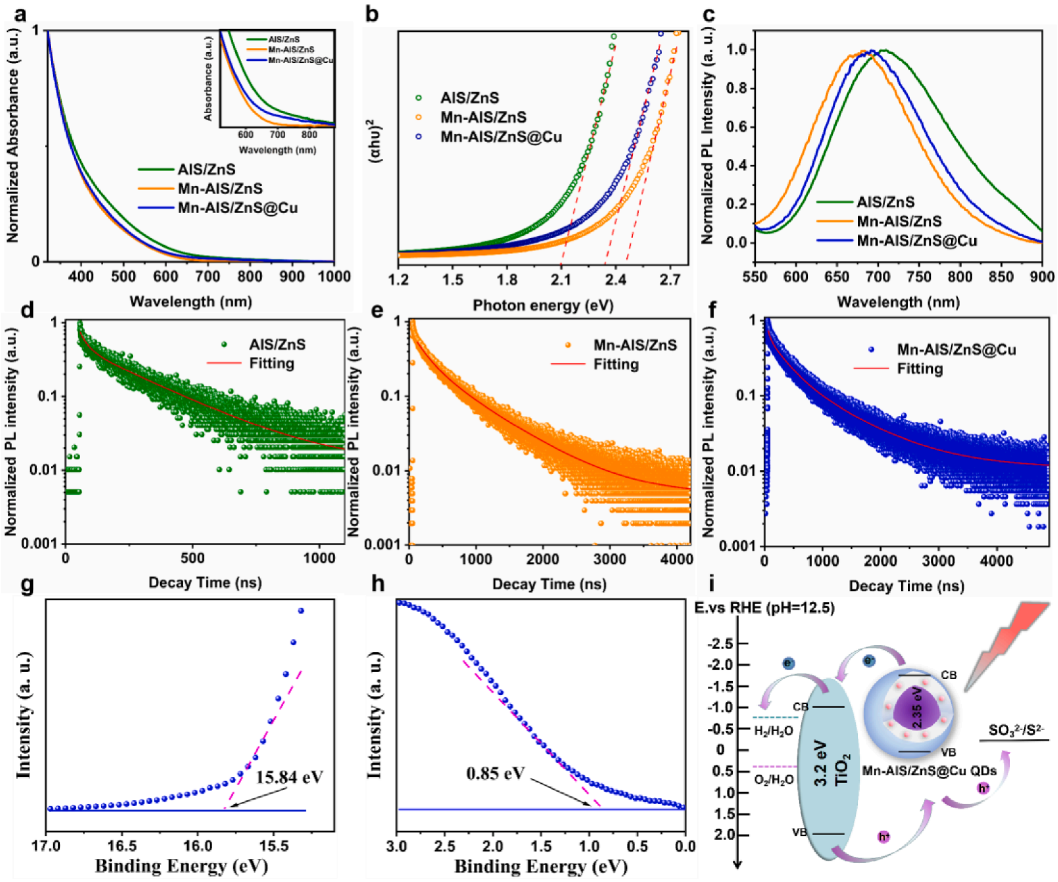

Fig. 2. (a) UV–vis absorption spectra of AIS/ZnS, Mn-AIS/ZnS and Mn-AIS/ZnS@Cu QDs. (b) Tauc plot curves for calculating E_g of QDs via extrapolation derived from a). (c) PL spectra and (d-f) Transient PL decay curves of AIS/ZnS, Mn-AIS/ZnS and Mn-AIS/ZnS@Cu QDs. High-resolution UPS spectra of Mn-AIS/ZnS@Cu QDs for (g) high and h) low binding energy cut-off. (i) Schematic band alignment of the Mn-AIS/ZnS@Cu QDs-decorated photoelectrode.

decay curves by a tri-exponential function and the average PL lifetimes of all QDs were calculated and tabulated in Table S2. Fig. 2**d** depicts an average PL lifetime of ~ 280 ns for AIS/ZnS QDs, while the Mn-AIS/ZnS QDs exhibited a largely prolonged average lifetime of ~ 560 ns (Fig. 2**e**) due to the leakage of electrons from core into the shell, which is caused by the Mn-alloying that enlarge the band gap of AIS core for decreased conduction band offset of Mn-AIS core with ZnS shell. The PL lifetimes of Mn-AIS/ZnS core/shell QDs are prone to extend with increasing Mn concentration, while an excessive amount of Mn alloying can result in the decreased PL lifetime (**Figure S7**), which is attributed to the emerging non-radiative recombination channels induced by the enhanced Mn–Mn coupling interactions.[56–57] After Cu-doping in the ZnS shell, the average PL lifetime of the Mn-AIS/ZnS@Cu QDs further prolonged to be ~ 620 ns (Fig. 2**f**), which is due to the effective spatial separation of electrons and holes in this core/shell structure, as a result of the hole capturing via Cu^+ states in the shell. Such hole capturing effect can also be verified by the prolonged average lifetime of Cu-doped AIS/ZnS QDs (~301 ns, **Figure S8**) with respect to the undoped AIS/ZnS QDs (~280 ns). However, a higher Cu dopants concentration can consequently give rise to the formation of hole scattering centers for decreased PL lifetime,[51] as illustrated in **Figure S9**. To summarize, the synergetic Mn and Cu modifications on AIS/ZnS core/shell QDs both optimize the optical properties of the composite structure and promote the corresponding charge carrier's transfer/separation, which is beneficial for the QDs-based solar energy conversion applications.

To assess the feasibility of as-obtained Mn-AIS/ZnS@Cu QDs in sensitizing photoelectrode (e.g. TiO_2), the band edge positions of this type of QDs were further determined via UV photoelectron spectroscopy (UPS, He I, 21.21 eV), as shown in **Figure S10 and** Fig. 2**g-h**. The high binding energy cut-off of Mn-AIS/ZnS@Cu QDs is measured to be 15.84 eV and the relevant Fermi level (E_f) is deduced as −5.37 eV in vacuum (E_{vac}). In parallel, the low binding energy cut-off (E_{lc}) of Mn-AIS/ZnS@Cu QDs is evaluated to be 0.85 eV. Using the obtained E_f and E_{lc} values, the position of valence band (VB) maximum (E_v) can be estimated as −6.22 eV relative to E_{vac}. Combining the band gap values of QDs from Tauc plots in Fig. 2**b** and E_v, the position of the conduction band (CB) minimum (E_c) vs E_{vac} can be calculated to be −3.87 eV. According to the band edge positions of TiO_2,[58] a type II band alignment is formed by assembling the Mn-AIS/ZnS@Cu QDs with TiO_2, which is conducive to the charge separation and transfer from QDs to TiO_2, as illustrated by the schematic diagram in Fig. 2**i**.

3.3. Morphology and charge dynamics of QDs-based photoanodes

A brief scheme for the fabrication processes of a QDs-sensitized photoanode is shown in Fig. 3**a**. Fig. 3**b** exhibits the cross-sectional scanning electron microscope (SEM) image of as-fabricated Mn-AIS/ZnS@Cu QDs/TiO_2 photoanode, in which the thickness of QDs-sensitized TiO_2 film was estimated to be ~ 16.2 μm. Fig. 3**c-k** show the EDS spectrum and elemental mapping of the Mn-AIS/ZnS@Cu QDs/TiO_2 photoanode, which confirm the existence of all compositions (Mn, Ag, In, S, Zn, Cu, Ti and O) and demonstrate the uniform distribution of Mn-AIS/ZnS@Cu QDs in the entire TiO_2 mesoporous film.

Accordingly, we proposed the insight effects of synergetic Mn and Cu modifications on the charge carrier dynamics in this core/shell QDs-TiO_2 heterostructure, as expressed in Fig. 3**l**. On one hand, although the AIS/ZnS core/shell QDs possess a type I electronic band structure, the Mn alloying can enlarge the band gap of AIS core and decrease the band

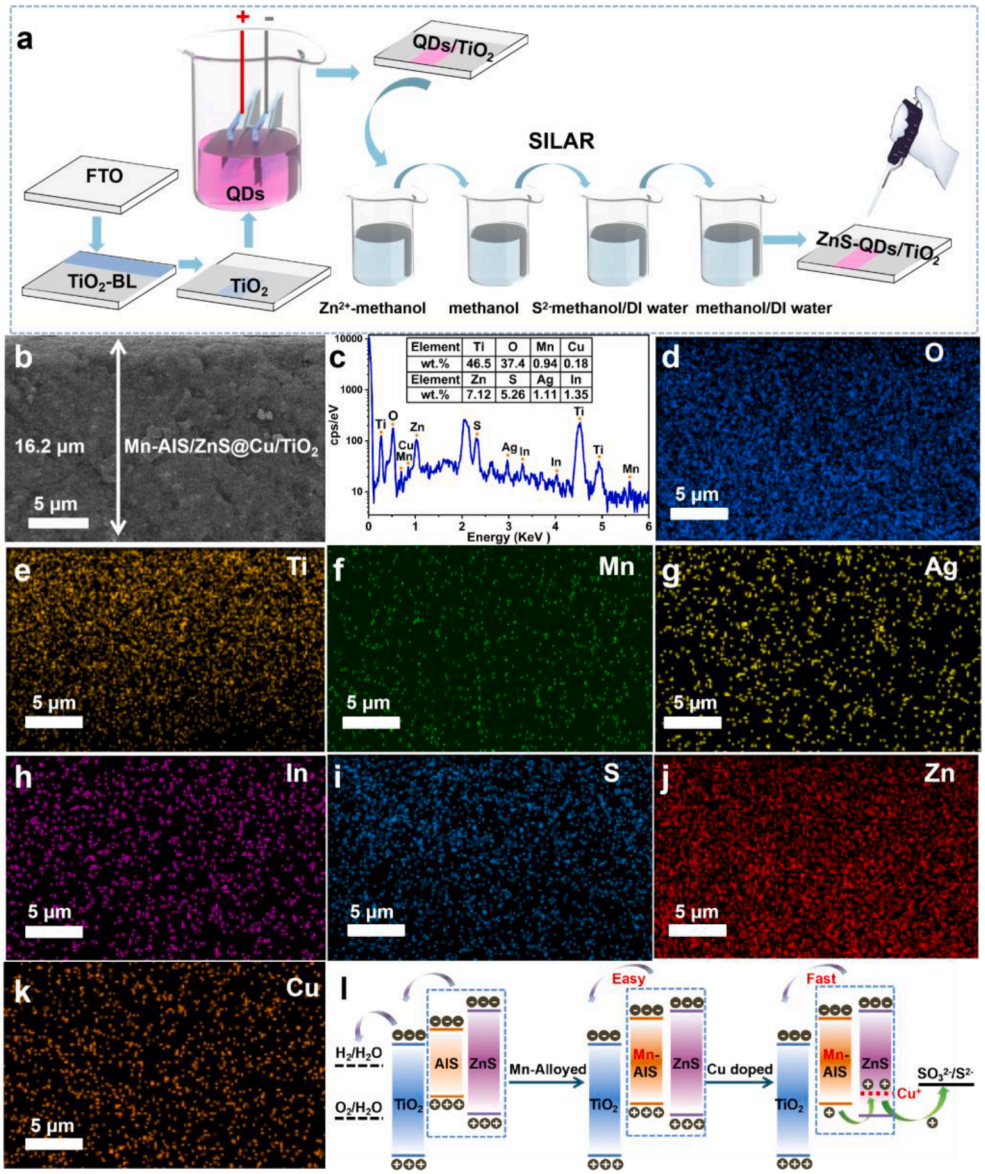

Fig. 3. (a) Scheme for fabrication processes of QDs-sensitized TiO_2 photoelectrode. (b) Cross-sectional SEM image, (c) EDS spectra and (d–k) corresponding EDS mapping (O, Ti, Mn, Ag, In, S, Zn and Cu) of Mn-AIS/ZnS@Cu core/shell QDs-sensitized TiO_2 photoelectrode. (l) The proposed insight charge dynamics mechanism of synergetic Mn and Cu modifications in Mn-AIS/ZnS@Cu QDs/TiO_2 heterostructure.

offset of the CB between Mn-AIS core and ZnS shell, thus facilitating the photo-induced electron transfer from core to shell region in QDs and improving the electron extraction efficiency from QDs to TiO_2. On the other hand, further doping of Cu into the ZnS shell can generate Cu^+ impurity states that effectively capture the photo-excited holes of core QDs, thereby accelerating the transfer rate of the holes to sacrificial agent in electrolyte and reducing the overall charge recombination in QDs.

To support this conclusion, the relevant charge carrier dynamics of QDs-TiO_2 heterostructures were further studied by using time-resolved PL spectra.[59–61] Using a typical benchmark system, we measured the PL lifetime of QDs/TiO_2 and QDs/ZrO_2 (with and without electrolyte) heterostructures, wherein we assumed no charge transfer occurring from QDs to ZrO_2 due to the extremely wide band gap (~6 eV) of ZrO_2 insulator. As-obtained PL lifetimes of TiO_2 and ZrO_2 deposited with different types of QDs were systematically compared to uncover the charge transfer kinetics (Fig. 4 **and** Figure S11). For all types of QDs, the PL lifetimes of QDs/TiO_2 decay much faster than that of the QDs/ZrO_2 heterostructures (Table S3), confirming the efficient charge transfer from QDs to TiO_2. Based on the average PL lifetime values of QDs/TiO_2 ($\tau_{QDs/TiO2}$) and QDs/ZrO_2 ($\tau_{QDs/ZrO2}$) heterostructures, we calculated the electron transfer rate (K_{et}) using the following equation [8]:

$$K_{et} = \frac{1}{\tau_{QDs/TiO_2}} - \frac{1}{\tau_{QDs/ZrO_2}} \quad (5)$$

According to calculation results in Table S3, the electron transfer rate of Mn-AIS/ZnS QDs-based photoelectrode (4.32×10^7 s^{-1}) is much higher than that of the unalloyed AIS/ZnS QDs (0.68×10^7 s^{-1}), demonstrating that the Mn-alloying in AIS/ZnS core/shell QDs can enhance the electron transfer from QDs to TiO_2 by band structure engineering. After Cu-doping, the electron transfer rate of Mn-AIS/ZnS@Cu QD-device (5.53×10^7 s^{-1}) is further improved to be higher than that of the Mn-AIS/ZnS QDs (4.32×10^7 s^{-1}), which indicates that introducing Cu^+ states in the ZnS shell enables the capture of the photo-excited holes from the core for boosted hole transfer rate and can inhibit charge recombination to further promote electron transfer from QDs to TiO_2.

The effect of Cu doping on the hole transfer rate was studied and

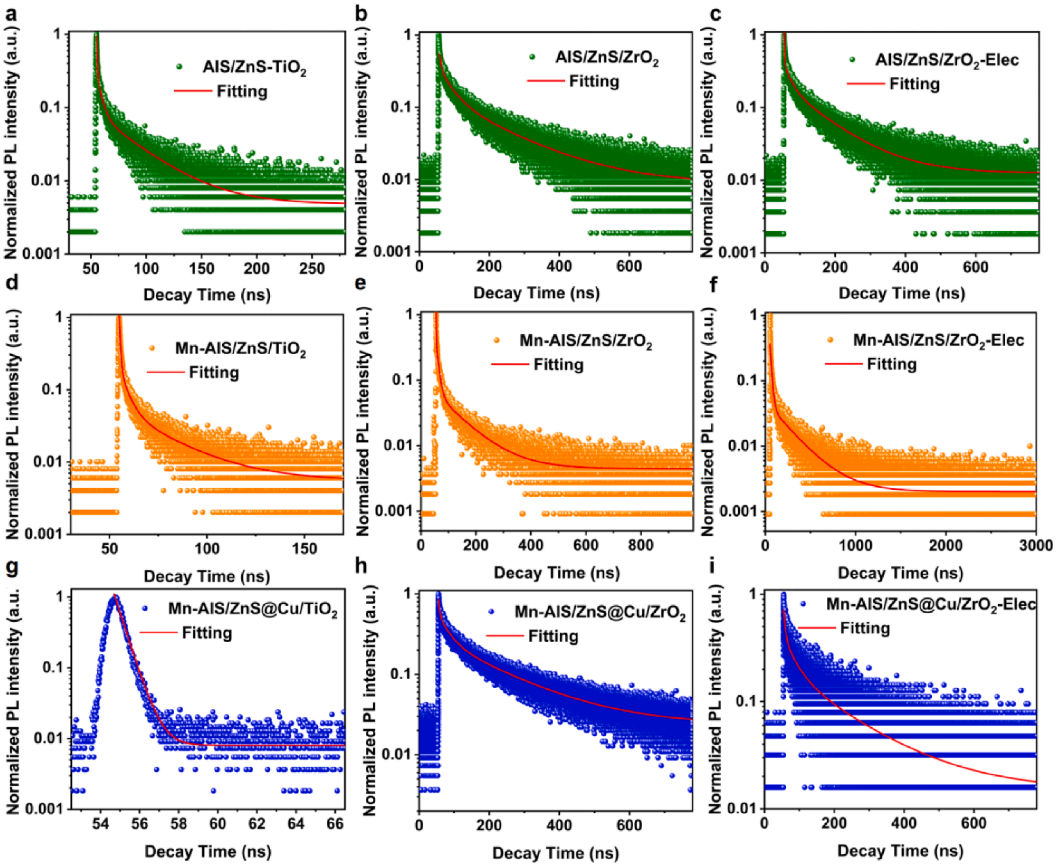

Fig. 4. Time-resolved PL decay curves of (a-c) AIS/ZnS, (d-f) Mn-AIS/ZnS and (g-i) Mn-AIS/ZnS@Cu QDs-coupled TiO_2 and ZrO_2 (with or without electrolyte).

verified via measuring the average lifetime of three kinds of QDs-ZrO_2 in the presence of electrolyte. The hole transfer rate was calculated based on the average lifetimes of QDs/ZrO_2 with and without electrolyte using the following equation:

$$K_{ht} = \frac{1}{\tau_{QDs/ZrO_2(electrolyte)}} - \frac{1}{\tau_{QDs/ZrO_2}} \quad (6)$$

As shown in Table S3, the calculated hole transfer rates (K_{ht}) of Mn-AIS/ZnS@Cu QDs-based photoanode ($0.71 \times 10^7\ s^{-1}$) and AIS/ZnS@Cu QDs ($0.46 \times 10^7\ s^{-1}$) are both higher than that of the undoped Mn-AIS/ZnS QDs ($0.27 \times 10^7\ s^{-1}$) and AIS/ZnS QDs ($0.18 \times 10^7\ s^{-1}$), respectively, thus confirming the positive effect of Cu-doping for boosted hole transfer in the QDs.

3.4. Performance of solar-driven QDs-based PEC cells

As-prepared QDs-TiO_2 photoanodes were subsequently applied as working electrodes in a typical three-electrode PEC cell for solar-driven hydrogen evolution, and the corresponding working principle of our QD-PEC cells is elaborated in Fig. 5**a**. After absorbing the incident light, the electrons (e^-) in the VB of QDs are excited to CB and leave behind the holes (h^+). Due to the formed type II band alignment of QDs and TiO_2, the photo-excited electrons can be effectively transferred to TiO_2, conductive substrate and then migrate to the counter Pt electrode for water reduction (i.e. H_2 production). Meanwhile, the photo-excited holes can move to the QD's surface to induce oxidation processes by reacting with the sacrificial agent in the electrolyte.

To evaluate the performance of as-assembled QDs-PEC devices, linear sweep voltammetry (LSV) tests of different QDs-based photoanodes were conducted in the dark, under 1 sun light and chopped illumination (AM 1.5G, 100 mW cm^{-2}). As shown in Fig. 5**b**, the AIS/ZnS QDs-TiO_2 photoelectrode exhibited a saturated photocurrent density of ~ 1.3 mA/cm^2, while the optimized Mn-AIS/ZnS QDs-TiO_2 photoelectrode delivered a significantly increased photocurrent density of ~ 4.8 mA cm^{-2} (Fig. 5**c**). The improved photocurrent density can be assigned to the Mn-alloying effect that tailors the band structure of AIS/ZnS core/shell QDs for enhanced photoexcited electrons transfer from QDs to TiO_2. To investigate the effect of Mn alloying concentration on the PEC performance of QDs-photoelectrodes, LSV tests on a series of Mn-AIS/ZnS QDs-TiO_2 photoelectrodes with variable Mn concentrations were conducted and shown in **Figure S12** and Table S2. With gradual increase of Mn content, the Mn-AIS/ZnS QDs-TiO_2 photoelectrodes exhibited improved photocurrent density due to the enhanced electron transfer, however, the excess amount of Mn can lead to decreased PEC performance (**Figure S12**) due to the reduced light absorption (**Figure S5a**) and emerging Mn-related non-radiative recombination in Mn-AIS core QDs, as evidenced by the largely reduced PL lifetime of Mn-AIS/ZnS QDs with the highest Mn contents (**Figure S7**).

As compared to the optimized photocurrent density of Mn-AIS/ZnS QDs-TiO_2 photoelectrode (~4.8 mA cm^{-2}), after further Cu shell doping, a higher saturated photocurrent density of ~ 6.4 mA cm^{-2} was attained for the Mn-AIS/ZnS@Cu QDs-TiO_2 photoanode (Fig. 5**d**). Such performance enhancement is attributed to both the accelerated electron transfer from QDs to TiO_2 and the improved holes transfer from QDs to electrolyte, as a result of the hole capturing effect from Cu^+ states in the shell. Nevertheless, over doping of Cu in the ZnS shell can lead to the decreased PEC performance of Mn-AIS/ZnS@Cu QDs-based PEC cell (**Figure S13**), which is due to the formation of new scattering centers and consistent with the decreased PL lifetime of the QDs with high Cu doping concentration.[49,53] Such hole capturing effect from Cu-doping can be further verified by comparing the PEC performance of AIS/ZnS@Cu and AIS/ZnS QDs-based photoelectrodes. As shown in **Figure S14**, the Cu-doped AIS/ZnS QDs-photoanode exhibited an enhanced photocurrent density of ~ 2.1 mA cm^{-2} than that of the

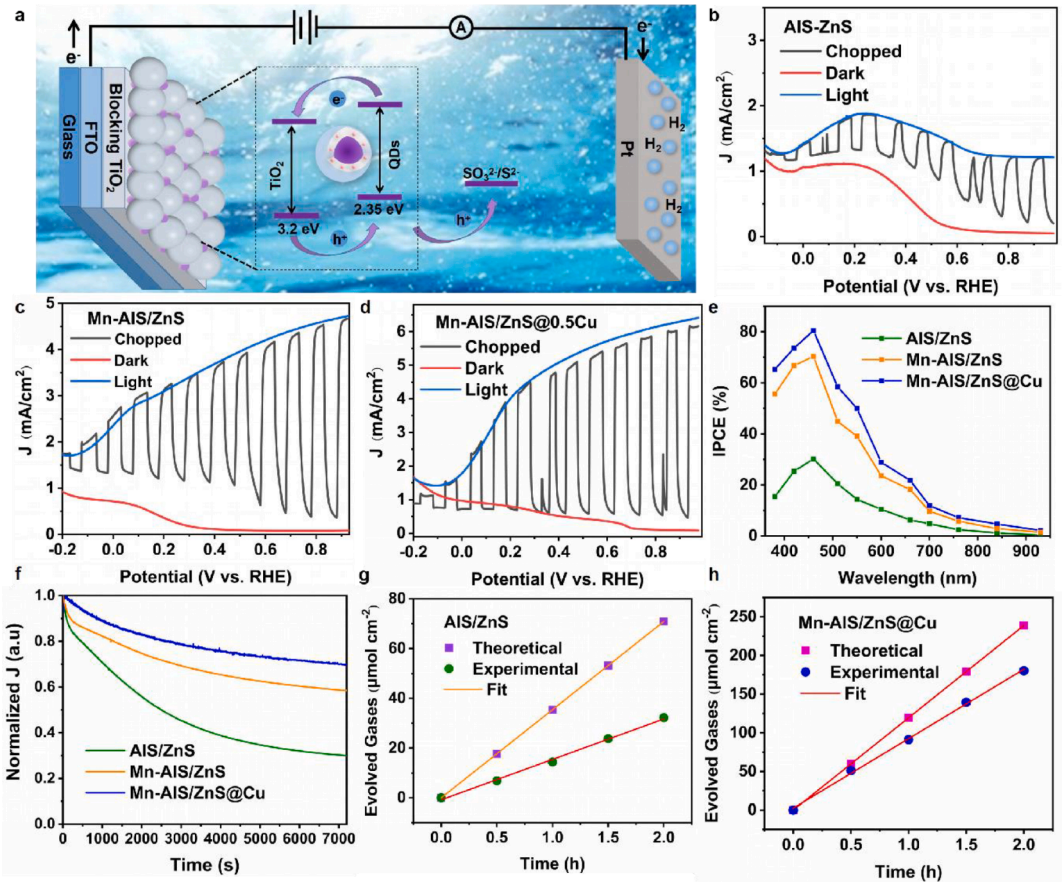

Fig. 5. (a) Scheme for solar light-driven QDs-based PEC H_2 evolution. *J–V* curves for (b) AIS/ZnS, (c) Mn-AIS/ZnS and (d) Mn-AIS/ZnS@Cu QDs-sensitized photoelectrodes in the dark, under light and chopped irradiation (AM 1.5G, 100 mW/cm^2). (e) IPCE spectra of all QDs-based photoanodes. (f) Normalized photocurrent density as a function of time for the AIS/ZnS/TiO_2, Mn-AIS/ZnS/TiO_2 and Mn-AIS/ZnS@Cu/TiO_2 photoelectrodes at 0.6 V vs. RHE. H_2 evolution as a function of time for (g) AIS/ZnS and h) Mn-AIS/ZnS@Cu QDs-PEC cells.

undoped AIS/ZnS QDs (~1.3 mA/cm^2), suggesting that doping Cu in the shell of AIS/ZnS QDs can indeed optimize the hole transfer for improved device performance. Moreover, without the use of sacrificial agents, the PEC performance of QDs-based photoelectrodes under neutral conditions was measured and shown in **Figure S15**, depicting photocurrent densities of ~ 0.8, 2.2 and 3.3 mA/cm^2 for AIS/ZnS, Mn-AIS/ZnS and Mn-AIS/ZnS@Cu QD samples, respectively.

The Mott-Schottky plots and electrochemical impedance spectroscopy (EIS) measurements were further conducted to analyze the charge dynamics processes in the QDs-PEC devices, as displayed in **Figure S16**. It can be observed that the Mott-Schottky plot of Mn-AIS/ZnS@Cu QDs-based device exhibits the lowest slope than that of the Mn-AIS/ZnS and AIS/ZnS QDs (**Figure S16a**), which indicates the highest donor density for improved conductivity and photoexcited electrons collection efficiency in Mn-AIS/ZnS@Cu QDs-based PEC cell. Similarly, the measured electrochemical impedance spectroscopy (EIS) Nyquist plots of these QDs-based photoanodes in **Figure S16b** also show a smaller semicircle radius of the Mn-AIS/ZnS@Cu QDs-based photoanode sample than other QDs-photoanodes, demonstrating a lower charge transfer resistance for the Mn-AIS/ZnS@Cu QDs-PEC device.

Incident photon to current conversion efficiency (IPCE) spectra of QDs-photoanodes were measured and shown in Fig. 5**e**. It can be observed that the Mn-AIS/ZnS@Cu QDs-based device exhibited higher IPCE values (from 400 to 800 nm) than that of the other QDs-device samples, which is consistent with its highest PEC performance. Moreover, the stability of these QDs-photoelectrodes under 2-hour light illumination was studied and the measured *J-t* curves are displayed in Fig. 5**f**. To better compare the decay trend for all QDs-photoanodes, we examine the normalized photocurrent density. After 2-hour continuous light illumination, the Mn-AIS/ZnS@Cu/TiO_2 photoelectrode demonstrated improved stability (maintaining ~ 70% of initial photocurrent) than the Mn-AIS/ZnS/TiO_2 (maintaining ~ 60% of initial photocurrent) and AIS/ZnS/TiO_2 (maintaining ~ 30% of initial photocurrent) samples. The improved stability can be mainly ascribed to the increased electron transfer and hole extraction in the core/shell QDs by synergistic Mn-alloying and Cu-doping, which result in the retarded charge recombination and reduced self-oxidation inside the QDs, thereby improving the stability of corresponding QDs-based PEC devices. Moreover, the device stability and long-term photocurrent density (after 2 h illumination) of our Mn-AIS/ZnS@Cu QDs-based PEC cells are comparable to the best-reported eco-friendly QDs-based PEC systems, with specific higher device stability than most of the Ag-based "green" QDs, as summarized in Table S4.

Gas chromatography (GC) system was further employed to detect and quantify the real H_2 production rate of as-assembled QD-PEC cells. Fig. 5**g** quantitatively shows the H_2 generation curves of AIS/ZnS QDs-TiO_2 photoelectrode, wherein the theoretical estimation of H_2 was obtained from *J-t* curve (**Figure S17**) and the actual H_2 generation rate was tested to be ~ 16.1 μmol cm^{-2}h^{-1}. Based on the theoretical and experimental amount of H_2, the Faraday efficiency (FE) of AIS/ZnS QDs-based photoanode was calculated to be ~ 45.4%. In comparison, the amount of H_2 evolution for Mn-AIS/ZnS@Cu QDs-based photoelectrode is depicted in Fig. 5**h**, showing a significantly boosted experimental H_2 productivity of 90.2 μmol cm^{-2}h^{-1}, which is about five folds higher than that of the AIS/ZnS QDs-device. The calculated FE for Mn-AIS/ZnS@Cu QDs-photoelectrode was ~ 75.5%, which is much higher than the FE of

AIS/ZnS QDs-device sample (~45.4%). Furthermore, the long-term hydrogen production performance up to 4 h for the Mn-AIS/ZnS@Cu QDs-based device was measured and shown in **Figure S18**. It was observed that the hydrogen production rate started to show decreasing trend after 3 h, while the average hydrogen production rate for 4 h illumination was still relatively high (~62.8 μmol $cm^{-2}h^{-1}$). These results demonstrate the great potential of Mn-AIS/ZnS@Cu QDs for highly efficient and stable PEC hydrogen evolution.

4. Conclusion and perspectives

In conclusion, we engineered the optoelectronic properties of environmentally friendly AIS/ZnS core/shell QDs via using synergistic Mn core alloying and Cu shell doping strategies and fabricated the corresponding "green" Mn-AIS/ZnS@Cu QDs-based PEC cells for light-driven H_2 production. It is found that the Mn-alloying in AIS/ZnS core/shell QDs can increase core's band gap and result in a smaller band offset between CB of Mn-AIS core and ZnS shell, thus promoting the electron "leakage" in the shell for prolonged PL lifetime and enhanced charge separation of QDs. Simultaneously, a further Cu-doping in the ZnS shell can introduce Cu^+ states that efficiently capture the holes from Mn-AIS core QDs, thus leading to inhibited charge recombination in the QDs and optimized charge transfer dynamics of relevant QDs-based PEC devices. As a result, by controlling the contents of Mn alloying and Cu doping, the optimized Mn-AIS/ZnS@Cu QDs-PEC cell can reach a photocurrent density as high as 6.4 mA cm^{-2} under one sun illumination (AM 1.5 G, 100 mW cm^{-2}). In addition, such Mn-AIS/ZnS@Cu QDs-based PEC device showed excellent durability, maintaining ~ 70% of its initial photocurrent value after 2-hour continuous light irradiation. The results indicate that synergistically tailoring core and shell materials of eco-friendly core/shell QDs is very promising to realize heavy metal-free, highly efficient and long-term stable QDs-based solar energy conversion devices. Future studies including step-wise band energy level formation in the core/shell QDs (i.e. interfacial layer engineering) and structure modification of QD-semiconductors for enhanced charge transfer (e.g. using 0D/2D architecture) are alternative research directions for further device performance optimizations.

Declaration of Competing Interest

The authors declare that they have no known competing financial interests or personal relationships that could have appeared to influence the work reported in this paper.

Acknowledgements

X.T. acknowledges the support from National Key Research and Development Program of China (No. 2019YFE0121600), National Natural Science Foundation of China (No. 22105031, 62011530131), Sichuan Science and Technology Program (No. 2021YFH0054) and Innovation Group Project of Sichuan Province (No. 20CXTD0090). Z.M. W. acknowledges the support from the "111 Project" (No. B20030). A.V. acknowledges the Knut & Alice Wallenberg Foundation and the Kempe Foundation for financial support.

Appendix A. Supplementary data

Supplementary data to this article can be found online at https://doi.org/10.1016/j.cej.2022.136214.

References

[1] C. McGlade, P. Ekins, The geographical distribution of fossil fuels unused when limiting global warming to 2 °C, Nature 517 (7533) (2015) 187–190.
[2] I. Dincer, Renewable energy and sustainable development: A crucial review, Renew. Sust. Energy Rev. 4 (2) (2000) 157–175.
[3] J. Li, S.K. Cushing, F. Meng, T.R. Senty, A.D. Bristow, N. Wu, Plasmon-induced resonance energy transfer for solar energy conversion, Nat. Photonics 9 (9) (2015) 601–607.
[4] H.G. Cha, K.-S. Choi, Combined biomass valorization and hydrogen production in a photoelectrochemical cell, Nat. Chem. 7 (4) (2015) 328–333.
[5] G. Hodes, D. Cahen, J. Manassen, Tungsten trioxide as a photoanode for a photoelectrochemical cell (PEC), Nature 260 (1976) 312–313.
[6] G. Hodes, A thin-film polycrystalline photoelectrochemical cell with 8% solar conversion efficiency, Nature 285 (5759) (1980) 29–30.
[7] P. Reiss, M. Protière, L. Li, Core/shell semiconductor nanocrystals, Small 5 (2) (2009) 154–168.
[8] Z. Long, X. Tong, C. Liu, A.I. Channa, R. Wang, X. Li, F. Lin, A. Vomiero, Z. M. Wang, Near-infrared, eco-friendly ZnAgInSe quantum dots-sensitized graphene oxide-TiO_2 hybrid photoanode for high performance photoelectrochemical hydrogen generation, Chem. Eng. J. 426 (2021), 131298.
[9] H.C. Fu, P. Varadhan, M.L. Tsai, W. Li, Q. Ding, C.H. Lin, M. Bonifazi, A. Fratalocchi, S. Jin, J.H. He, Improved performance and stability of photoelectrochemical water-splitting Si system using a bifacial design to decouple light harvesting and electrocatalysis, Nano Energy 70 (2020), 104478.
[10] X. Li, C. Gao, H. Duan, B. Lu, X. Pan, E. Xie, Nanocrystalline TiO_2 film based photoelectrochemical cell as self-powered UV-photodetector, Nano Energy 1 (4) (2012) 640–645.
[11] S. Zhang, Z. Liu, M. Ruan, Z. Guo, E. Lei, W. Zhao, D. Zhao, X. Wu, D. Chen, Enhanced piezoelectric-effect-assisted photoelectrochemical performance in ZnO modified with dual cocatalysts, Appl. Catal. B-Environ. 262 (2020), 118279.
[12] A. Kargar, Y.i. Jing, S.J. Kim, C.T. Riley, X. Pan, D. Wang, ZnO/CuO heterojunction branched nanowires for photoelectrochemical hydrogen generation, ACS Nano 7 (12) (2013) 11112–11120.
[13] L. Liccardo, E. Lushaj, L. Dal Compare, E. Moretti, A. Vomiero, Nanoscale ZnO/α-Fe_2O_3 heterostructures: toward efficient and low-cost photoanodes for water splitting, Small, Science (2021) 2100104.
[14] R. Mazzaro, S.B. Bibi, M. Natali, G. Bergamini, V. Morandi, P. Ceroni, A. Vomiero, Hematite nanostructures: An old material for a new story, Simultaneous photoelectrochemical oxidation of benzylamine and hydrogen production through Ti doping, Nano Energy 61 (2019) 36–46.
[15] K. Qi, B. Cheng, J. Yu, W. Ho, A review on TiO_2-based Z-scheme photocatalysts, Chinese J Catal. 38 (12) (2017) 1936–1955.
[16] J.-Y. Xu, X. Tong, L.V. Besteiro, X. Li, C. Hu, R. Liu, A.I. Channa, H. Zhao, F. Rosei, A.O. Govorov, Q. Wang, Z.M. Wang, Rational synthesis of novel "giant" CuInTeSe/CdS core/shell quantum dots for optoelectronics, Nanoscale 13 (36) (2021) 15301–15310.
[17] B.-R. Hyun, Y.-W. Zhong, A.C. Bartnik, L. Sun, H.D. Abruña, F.W. Wise, J. D. Goodreau, J.R. Matthews, T.M. Leslie, N.F. Borrelli, Electron injection from colloidal PbS quantum dots into titanium dioxide nanoparticles, ACS Nano 2 (11) (2008) 2206–2212.
[18] Y. Yan, R.W. Crisp, J. Gu, B.D. Chernomordik, G.F. Pach, A.R. Marshall, J. A. Turner, M.C. Beard, Multiple exciton generation for photoelectrochemical hydrogen evolution reactions with quantum yields exceeding 100%, Nat. Energy 2 (2017) 1–7.
[19] L. Jin, G. Sirigu, X. Tong, A. Camellini, A. Parisini, G. Nicotra, C. Spinella, H. Zhao, S. Sun, V. Morandi, M.Z. Rossi, F. Rosei, A. Vomiero, Engineering interfacial structure in "Giant" PbS/CdS quantum dots for photoelectrochemical solar energy conversion, Nano Energy 30 (2016) 531–541.
[20] W.W. Zhao, R. Chen, P.P. Dai, X.L. Li, J.J. Xu, H.Y. Chen, A general strategy for photoelectrochemical immunoassay using an enzyme label combined with a CdS quantum dot/TiO_2 nanoparticle composite electrode, Anal. Chem. 86 (2014) 11513–11516.
[21] J. Feng, F. Li, X. Li, X. Ren, D. Fan, D. Wu, H. Ma, B. Du, N. Zhang, Q. Wei, An amplification label of core–shell CdSe@ CdS QD sensitized GO for a signal-on photoelectrochemical immunosensor for amyloid β-protein, J. Mater. Chem. B 7 (7) (2019) 1142–1148.
[22] V. Veeramani, Y.H. Chen, H.C. Wang, T.F. Hung, W.S. Chang, D. Wei, S. Hu, R. Liu, CdSe/ZnS QD@ CNT nanocomposite photocathode for improvement on charge overpotential in photoelectrochemical Li-O_2 batteries, Chem. Eng. J. 349 (2018) 235–240.
[23] W.X. Dai, L. Zhang, W.W. Zhao, X.D. Yu, J.J. Xu, H.Y. Chen, Hybrid PbS quantum dot/nanoporous NiO film nanostructure: preparation, characterization, and application for a self-powered cathodic photoelectrochemical biosensor, Anal. Chem. 89 (2017) 8070–8078.
[24] X. Tong, A.I. Channa, Y. You, P. Wei, X. Li, F. Lin, J. Wu, A. Vomiero, Z.M. Wang, Boosting the performance of eco-friendly quantum dots-based photoelectrochemical cells via effective surface passivation, Nano Energy 76 (2020), 105062.
[25] A.C. Berends, M.J.J. Mangnus, C. Xia, F.T. Rabouw, C. de Mello Donega, Optoelectronic properties of ternary I-III–VI_2 semiconductor nanocrystals: bright prospects with elusive origins, J. Phys. Chem. Lett. 10 (2019) 1600–1616.
[26] F. Li, M. Zhang, D. Benetti, L. Shi, L.V. Besteiro, H. Zhang, J. Liu, G.S. Selopal, S. Sun, Z.M. Wang, Q. Wei, F. Rosei, "Green", gradient multi-shell $CuInSe_2$/$(CuInSe_xS_{1-x})_5$/$CuInS_2$ quantum dots for photo-electrochemical hydrogen generation, Appl. Catal. B-Environ. 280 (2021), 119402.
[27] F. Zhang, Y. Chen, W. Zhou, C. Ren, H. Gao, G. Tian, Hierarchical SnS_2/$CuInS_2$ nanosheet heterostructure films decorated with C_{60} for remarkable photoelectrochemical water splitting, ACS Appl. Mater. Inter. 11 (2019) 9093–9101.

[28] L. Wang, W. Gu, P. Sheng, Z. Zhang, B. Zhang, Q. Cai, Sensor. A label-free cytochrome c photoelectrochemical aptasensor based on CdS/$CuInS_2$/Au/TiO_2 nanotubes, Actuat. B-Chem. 281 (2019) 1088–1096.
[29] K. Wang, X. Tong, Y. Zhou, H. Zhang, F. Navarro-Pardo, G.S. Selopal, G. Liu, J. Tang, Y. Wang, S. Sun, D. Ma, Z. Wang, F. Vidal, H. Zhao, X. Sun, F. Rosei, Efficient solar-driven hydrogen generation using colloidal heterostructured quantum dots, J. Mater. Chem. A 7 (23) (2019) 14079–14088.
[30] G. Wang, H. Wei, J. Shi, Y. Xu, H. Wu, Y. Luo, D. Li, Q. Meng, Significantly enhanced energy conversion efficiency of $CuInS_2$ quantum dot sensitized solar cells by controlling surface defects, Nano Energy 35 (2017) 17–25.
[31] X. Hu, Q. Zhang, X. Huang, D. Li, Y. Luo, Q. Meng, Aqueous colloidal $CuInS_2$ for quantum dot sensitized solar cells, J. Mater. Chem. 21 (2011) 15903–15905.
[32] H. Rao, M. Zhou, Z. Pan, X. Zhong, Quantum dot materials engineering boosting the quantum dot sensitized solar cell efficiency over 13%, J. Mater. Chem. A 8 (20) (2020) 10233–10241.
[33] H. Song, Y.u. Lin, Z. Zhang, H. Rao, W. Wang, Y. Fang, Z. Pan, X. Zhong, Improving the efficiency of quantum dot sensitized solar cells beyond 15% via secondary deposition, J. Am. Chem. Soc. 143 (12) (2021) 4790–4800.
[34] H. Song, Y. Lin, M. Zhou, H. Rao, Z. Pan, X. Zhong, Zn-Cu-In-S-Se quinary "green" alloyed quantum-dot-sensitized solar cells with a certified efficiency of 14.4%, Angew. Chem. Int. Edit. 60 (2021) 6137–6144.
[35] D. Voigt, M. Bredol, A. Gonabadi, A general strategy for $CuInS_2$ based quantum dots with adjustable surface chemistry, Opt. Mater. 15 (2021), 110994.
[36] H. Guan, S. Zhao, H. Wang, D. Yan, M. Wang, Z. Zang, Room temperature synthesis of stable single silica-coated CsPbBr 3 quantum dots combining tunable red emission of Ag-In-Zn-S for High-CRI white light-emitting diodes, Nano Energy 67 (2020), 104279.
[37] P. Chuang, C. Lin, R. Liu, Emission-tunable $CuInS_2$/ZnS quantum dots: structure, optical properties, and application in white light-emitting diodes with high color rendering index, ACS Appl. Mater. Inter. 6 (2014) 15379–15387.
[38] J. Tang, K.W. Kemp, S. Hoogland, K.S. Jeong, H. Liu, L. Levina, M. Furukawa, X. Wang, R. Debnath, D. Cha, K.W. Chou, A. Fischer, A. Amassian, J.B. Asbury, E. H. Sargent, Colloidal-quantum-dot photovoltaics using atomic-ligand passivation, Nat. Mater. 10 (10) (2011) 765–771.
[39] D.O. Scanlon, C.W. Dunnill, J. Buckeridge, S.A. Shevlin, A.J. Logsdail, S. M. Woodley, C.R.A. Catlow, M.J. Powell, R.G. Palgrave, I.P. Parkin, G.W. Watson, T.W. Keal, P. Sherwood, A. Walsh, A.A. Sokol, Band alignment of rutile and anatase TiO_2, Nat. Mater. 12 (9) (2013) 798–801.
[40] X. Li, X. Tong, S. Yue, C. Liu, A.I. Channa, Y. You, R. Wang, Z. Long, Z. Zhang, Z. Zhao, X. Liu, Z.M. Wang, Rational design of colloidal $AgGaS_2$/CdSeS core/shell quantum dots for solar energy conversion and light detection, Nano Energy 89 (2021), 106392.
[41] A. Raevskaya, V. Lesnyak, D. Haubold, V. Dzhagan, O. Stroyuk, N. Gaponik, A. Eychmuller, A fine size selection of brightly buminescent water-soluble Ag-In-S and Ag-In-S/ZnS quantum dots, J. Phys. Chem. C 121 (2017) 9032–9042.
[42] X. Kang, Y. Yang, L. Wang, S. Wei, D. Pan, Warm white light emitting diodes with gelatin-coated $AgInS_2$/ZnS core/shell quantum dots, ACS Appl. Mater. Inter. 7 (50) (2015) 27713–27719.
[43] S.M. Kobosko, D.H. Jara, P.V. Kamat, $AgInS_2$-ZnS quantum dots: excited state interactions with TiO_2 and photovoltaic performance, ACS Appl. Mater. Inter. 9 (2017) 33379–33388.
[44] M.D. Regulacio, K.Y. Win, S.L. Lo, S.Y. Zhang, X. Zhang, S. Wang, Y. Zheng, Aqueous synthesis of highly luminescent $AgInS_2$–ZnS quantum dots and their biological applications, Nanoscale 5 (2013) 2322–2327.
[45] P. Kowalik, S.G. Mucha, K. Matczyszyn, P. Bujak, L.M. Mazur, A. Ostrowski, A. Kmita, M. Gajewska, A. Pron, Heterogeneity induced dual luminescence properties of $AgInS_2$ and $AgInS_2$-ZnS alloyed nanocrystals, Inorg. Chem. Front. 8 (14) (2021) 3450–3462.
[46] T. Torimoto, T. Adachi, K.-I. Okazaki, M. Sakuraoka, T. Shibayama, B. Ohtani, A. Kudo, S. Kuwabata, Facile synthesis of ZnS-$AgInS_2$ solid solution nanoparticles for a color-adjustable luminophore, J. Am. Chem. Soc. 129 (41) (2007) 12388–12389.
[47] G. Manna, S. Jana, R. Bose, N. Pradhan, Mn-doped multinary CIZS and AIZS nanocrystals, J. Phys. Chem. Lett. 3 (18) (2012) 2528–2534.
[48] R. Wang, X. Tong, A.I. Channa, Q. Zeng, J. Sun, C. Liu, X. Li, J. Xu, F. Lin, G. S. Selopal, F. Rosei, Y. Zhang, J. Wu, H. Zhao, A. Vomiero, X. Sun, Z.M. Wang, Environmentally friendly Mn-alloyed core/shell quantum dots for high-efficiency photoelectrochemical cells, J. Mater. Chem. A 8 (21) (2020) 10736–10741.
[49] J.G. Radich, R. Dwyer, P.V. Kamat, Cu_2S reduced graphene oxide composite for high-efficiency quantum dot solar cells. Overcoming the redox limitations of S_2/S_n^2 at the counter electrode, J. Phys. Chem. Lett. 2 (2011) 2453–2460.
[50] A. Nag, S. Chakraborty, D.D. Sarma, To dope Mn^{2+} in a semiconducting nanocrystal, J. Am. Chem. Soc. 130 (32) (2008) 10605–10611.
[51] J. Bang, S. Das, E.J. Yu, K. Kim, H. Lim, S. Kim, J.W. Hong, Controlled photoinduced electron transfer from InP/ZnS quantum dots through Cu doping: a new prototype for the visible-light photocatalytic hydrogen evolution reaction, Nano Lett. 20 (2020) 6263–6271.
[52] Q. Liu, R. Deng, X. Ji, D. Pan, Alloyed Mn-Cu-In-S nanocrystals: a new type of diluted magnetic semiconductor quantum dots, Nanotechnology 23 (2012), 255706.
[53] J.L. Shay, B. Tell, L.M. Schiavone, H.M. Kasper, F. Thiel, Synthesis and photophysical properties of ternary I-III-VI $AgInS_2$ nanocrystals: intrinsic versus surface states, Phys. Rev. B 9 (1972) 1719.
[54] H. Zhao, X. Li, M. Cai, C. Liu, Y. You, R. Wang, Z.M. Wang, Role of copper doping in heavy metal-free InP/ZnSe core/shell quantum dots for highly efficient and stable photoelectrochemical cell, Adv. Energy Mater. 11 (2021) 2101230.
[55] M. Lim, W. Lee, G. Bang, W.J. Lee, Y. Park, Y. Kwon, Y. Jung, S. Kim, J. Bang, Synthesis of far-red- and near-infrared-emitting Cu-doped InP/ZnS (core/shell) quantum dots with controlled doping steps and their surface functionalization for bioconjugation, Nanoscale 11 (21) (2019) 10463–10471.
[56] G. Halder, S. Bhattacharyya, Plight of Mn doping in colloidal CdS quantum dots to boost the efficiency of solar cells, J. Phys. Chem. C 119 (24) (2015) 13404–13412.
[57] Y. Liu, J. Zhang, B. Han, X. Wang, Z. Wang, C. Xue, G. Bian, D. Hu, R. Zhou, D.-S. Li, Z. Wang, Z. Ouyang, M. Li, T. Wu, New insights into Mn-Mn coupling interaction-directed photoluminescence quenching mechanism in Mn^{2+}-doped semiconductors, J. Am. Chem. Soc. 142 (14) (2020) 6649–6660.
[58] J. Chen, H.B. Yang, H.B. Tao, L. Zhang, J. Miao, H.Y. Wang, J. Chen, H. Zhang, B. Liu, Surface rutilization of anatase TiO_2 nanorods for creation of synergistically bridging and fencing electron highways, Adv. Funct. Mater. 26 (2015) 456–465.
[59] G.S. Selopal, H. Zhao, X. Tong, D. Benetti, F.N. Pardo, Y. Zhou, D. Barba, F. Vidal, Z.M. Wang, F. Rosei, Highly stable colloidal "giant" quantum dots sensitized solar cells, Adv. Funct. Mater. 27 (2017) 1701468.
[60] R. Adhikari, L. Jin, F.N. Pardo, D. Benetti, B. AlOtaibi, S. Vanka, H. Zhao, Z. Mi, A. Vomiero, F. Rosei, Pt-free photoelectrochemical cells for solar hydrogen generation based on "giant" quantum dots, Nano Energy 27 (2016) 265–274.
[61] H. Zhao, Z. Fan, H. Liang, G.S. Selopal, B.A. Gonfa, L. Jin, A. Soudi, D. Cui, F. Enrichi, M.M. Natile, I. Concina, D. Ma, A.O. Govorov, F. Rosei, A. Vomiero, Controlling photoinduced electron transfer from PbS@CdS core@shell quantum dots to metal oxide nanostructured thin films, Nanoscale 6 (12) (2014) 7004–7011.